The Dynamics of Mountain-Wave-Induced Rotors

JAMES D. DOYLE

Naval Research Laboratory, Monterey, California

DALE R. DURRAN

Department of Atmospheric Sciences, University of Washington, Seattle, Washington

(Manuscript received 28 February 2001, in final form 23 July 2001)

ABSTRACT

The development of rotor flow associated with mountain lee waves is investigated through a series of high-resolution simulations with the nonhydrostatic Coupled Ocean–Atmospheric Mesoscale Prediction System (COAMPS) model using free-slip and no-slip lower boundary conditions. Kinematic considerations suggest that boundary layer separation is a prerequisite for rotor formation. The numerical simulations demonstrate that boundary layer separation is greatly facilitated by the adverse pressure gradients associated with trapped mountain lee waves and that boundary layer processes and lee-wave-induced perturbations interact synergistically to produce low-level rotors. Pairs of otherwise identical free-slip and no-slip simulations show a strong correlation between the strength of the lee-wave-induced pressure gradients in the free-slip simulation and the strength of the reversed flow in the corresponding no-slip simulation.

Mechanical shear in the planetary boundary layer is the primary source of a sheet of horizontal vorticity that is lifted vertically into the lee wave at the separation point and carried, at least in part, into the rotor itself. Numerical experiments show that high shear in the boundary layer can be sustained without rotor development when the atmospheric structure is unfavorable for the formation of trapped lee waves. Although transient rotors can be generated with a free-slip lower boundary, realistic rotors appear to develop only in the presence of surface friction.

In a series of simulations based on observational data, increasing the surface roughness length beyond values typical for a smooth surface ($z_0 = 0.01$ cm) decreases the rotor strength, although no rotors form when free-slip conditions are imposed at the lower boundary. A second series of simulations based on the same observational data demonstrate that increasing the surface heat flux above the lee slope increases the vertical extent of the rotor circulation and the strength of the turbulence but decreases the magnitude of the reversed rotor flow.

1. Introduction

Mountain waves forced by long quasi-two-dimensional ridges are often accompanied by low-level vortices with horizontal axes parallel to the ridgeline. These horizontal vortices, known as rotors, were first documented by glider pilots in pioneering studies by Kuettner (1938, 1939). Mountain-wave-induced rotors can be severe aeronautical hazards and have been cited as contributing to numerous aircraft upsets and accidents, including occasional fatal accidents involving modern commercial and military aircraft (e.g., NTSB 1992). In addition to posing a significant aviation hazard, rotor circulations also may have an important impact on the transport of aerosols and chemical and biological contaminants in mountainous terrain. Nevertheless, in spite of their obvious importance, the dynamics of mountain-wave-induced rotors remains poorly understood.

One of the best observations of the structure of severe terrain-induced rotors was obtained from aircraft measurements over Owens Valley, California, on 16 February 1952 during the Sierra Wave Experiment (Holmboe and Klieforth 1957). The airflow pattern derived from in situ measurements collected on this day is shown in Fig. 1. Although not indicated on the figure, severe turbulence was encountered in the vicinity of the rotor cloud. More recently, Doppler lidar observations have provided a detailed description of flow in mountain-wave-induced rotors. One of the most clearly documented examples is shown in Fig. 7 of Ralph et al. (1997). Under the assumption that the flow is nondivergent in the two-dimensional vertical plane scanned by the lidar beam, the authors deduced the presence of a weak rotor associated with a trapped mountain lee wave in which a 500-m-deep surface-based reversed flow achieved a maximum upstream-directed velocity of 2.5 m s^{-1}.

Corresponding author address: James D. Doyle, Marine Meteorology Division, Naval Research Laboratory, 7 Grace Hopper Ave., Monterey, CA 93943-5502.
E-mail: doyle@nrlmry.navy.mil

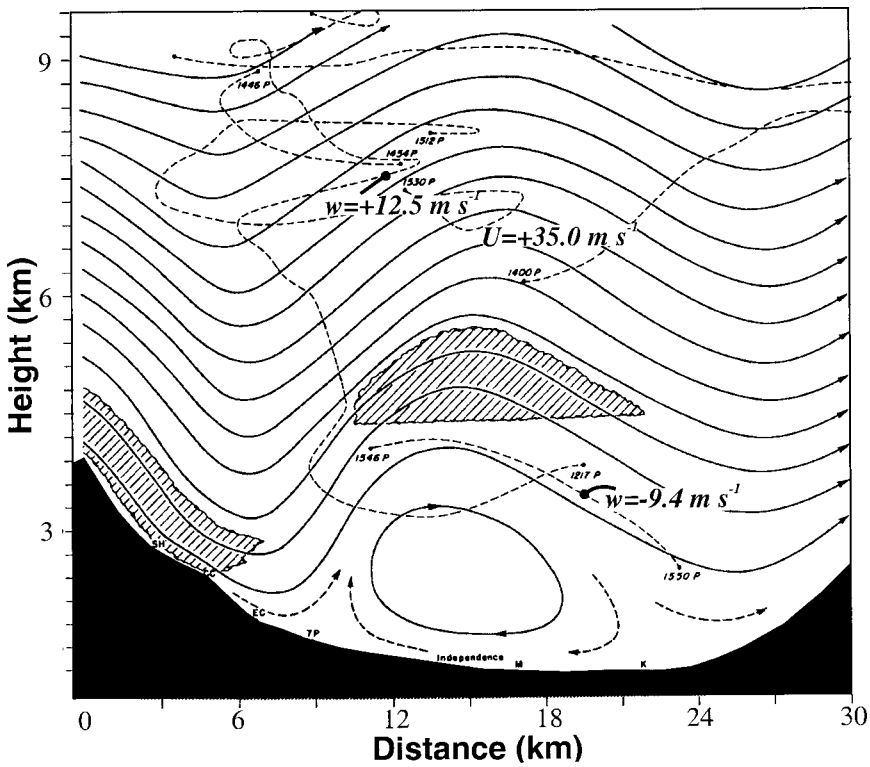

FIG. 1. Streamlines based on glider measurements during the Sierra Wave Project on 16 Feb 1952 (after Holmboe and Klieforth 1957).

Early theoretical investigations of rotor dynamics are reviewed in Queney et al. (1960). Lyra (1943) noted that the pressure perturbations associated with trapped mountain lee waves will tend to produce regions of adverse pressure gradient favorable for the formation of low-level rotor circulations. Out of necessity, Lyra's model relied on linear theory and ignored the planetary boundary layer. Kuettner (1959) avoided the linearity assumption by using a hydraulic model in which atmospheric rotors are represented by the hydraulic jumps that may form downstream of the crest in shallow-water flow over an obstacle. Kuettner added an idealized description of surface diabatic heating to the standard shallow-water model and suggested that lee-slope heating could account for the observation that the tops of the rotors encountered during the Sierra Wave Experiment typically extended above the height of the lowest layer delineated by the cap cloud over the mountain crests. Although advective nonlinearities are included in Kuettner's model, the use of shallow-water hydraulic theory does require a substantial approximation to the atmosphere's true vertical structure and the neglect of nonhydrostatic perturbations (like trapped lee waves). Moreover, since the horizontal velocity is independent of depth in a single-layer shallow water model, Kuettner's approach is not capable of explicitly resolving the reversal of the horizontal wind with height characteristic of an actual rotor.

With the exception of the recent study by Clark et al. (2000), which focused on horizontal vortex tubes and clear-air turbulence in wave-breaking regions in the upper troposphere, there appears to have been relatively little effort to investigate the dynamics of mountain-wave-induced rotors with modern numerical models. Such an effort is undertaken in this study; we apply a nonhydrostatic numerical model in order to examine the low-level rotors induced by an infinitely long ridge. In summarizing a large number of rotor observations, Queney et al. (1960) stated that ''rotor clouds seem to be the natural consequence of very large amplitude lee waves.'' The focus of this study will therefore be on atmospheric structures favorable to the development of trapped mountain lee waves, but in contrast to most previous theoretical investigations of such waves, we will explicitly consider the dynamical influence of the planetary boundary layer. Our focus on the boundary layer is partly motivated by the simple observation that the existence of reversed low-level flow at the base of a rotor suggests a link between rotor formation and boundary layer separation (Scorer 1955).[1] The same link is also suggested by the classic photograph of rotor clouds in the lee of the Sierra Nevada shown in Fig. 2.

[1] We use the term ''boundary layer separation'' to describe a rapid increase in the depth of the planetary boundary layer along a horizontal axis parallel to the velocity in the overlying airstream.

Dust picked up by the high surface winds blowing from right to left in Fig. 2 travels along near the surface until entering the rotor, at which point the boundary layer thickens rapidly as the flow breaks into chaotic turbulent eddies and rises into the rotor clouds.

In this study, a nonhydrostatic numerical model, initialized with both idealized and observed soundings, is used to explore the dynamics of mountain-wave-induced rotors. The numerical model is described in section 2. The results of idealized two-layer simulations are presented in section 3. Section 4 contains a discussion of surface drag and surface heating effects on rotors that develop in more realistic atmospheric conditions. The summary and conclusions are presented in section 5.

2. Numerical model description

The atmospheric portion of the Naval Research Laboratory's Coupled Ocean–Atmospheric Mesoscale Prediction System (COAMPS) (Hodur 1997), which makes use of finite-difference approximations to represent the fully compressible, nonhydrostatic equations that govern atmospheric motions, is used in this study. The Coriolis force is neglected here because of the high Rossby number flow considered. In this application, the model is applied in a two-dimensional mode with moist effects not included. Terrain is incorporated through a transformation to the following coordinate:

$$\sigma = \frac{z_t(z - h)}{z_t - h}, \tag{1}$$

where z_t is the depth of the model computation domain, z is the physical height, h is the terrain elevation, and σ is the transformed vertical coordinate. Under this transformation, the prognostic equations for the horizontal velocity u, vertical velocity w, perturbation Exner function π, and potential temperature θ are

$$\frac{Du}{Dt} + c_p\theta\left(\frac{\partial\pi}{\partial x} + G_x\frac{\partial\pi}{\partial\sigma}\right) = D_u, \tag{2}$$

$$\frac{Dw}{Dt} + c_p\theta G_z\frac{\partial\pi}{\partial\sigma} = g\frac{\theta - \overline{\theta}}{\overline{\theta}} + D_w, \tag{3}$$

$$\frac{D\pi}{Dt} + \dot{\sigma}\frac{\partial\overline{\Pi}}{\partial\sigma} + \frac{R}{c_v}(\overline{\Pi} + \pi)\left(\frac{\partial u}{\partial x} + G_x\frac{\partial u}{\partial\sigma} + G_z\frac{\partial w}{\partial\sigma}\right) - \frac{R}{c_v}\frac{(\overline{\Pi} + \pi)}{\theta}\frac{D\theta}{Dt} = 0, \tag{4}$$

$$\frac{D\theta}{Dt} = D_\theta, \tag{5}$$

where

$$(\overline{\Pi} + \pi) = \left(\frac{p}{p_0}\right)^{R/C_p}, \qquad \frac{D}{Dt} = \frac{\partial}{\partial t} + u\frac{\partial}{\partial x} + \dot{\sigma}\frac{\partial}{\partial\sigma},$$

$$G_x = \frac{\partial\sigma}{\partial x}, \qquad G_z = \frac{\partial\sigma}{\partial z},$$

$$\dot{\sigma} = G_x u + G_z w,$$

and $\overline{\theta}(z)$ is the mean potential temperature in hydrostatic balance with the mean Exner function $\overline{\Pi}(z)$, p_0 is 1000 hPa, R is the gas constant for dry air, c_p is specific heat for dry air at constant pressure, c_v is specific heat at constant volume, and the terms D_u, D_w, and D_θ represent the subgrid-scale vertical mixing and horizontal smoothing. The horizontal advection is represented by fourth-order accurate differencing, while second-order differencing is used to represent the vertical advection, pressure gradient, and divergence terms. A fourth derivative hyper-diffusion is used to control nonlinear instability. A time-splitting technique that features a semi-implicit treatment for the vertically propagating acoustic waves is used to efficiently integrate the compressible equations (Klemp and Wilhelmson 1978; Durran and Klemp 1983). The time differencing is centered for the large time step.

The subgrid-scale mixing for variable β is parameterized as $\overline{(w'\beta')} = -K\partial\beta/\partial z$, where K is the eddy-mixing coefficient defined as $S\ell e^{0.5}$. The mixing length ℓ is formulated based on Mellor and Yamada (1974) and Thompson and Burk (1991). The coefficient S is specified following Yamada (1983). The prognostic equation for the turbulent kinetic energy (TKE), $e = 1/2(\overline{u'^2} + \overline{w'^2})$ is based on the level 2.5 formulation of Mellor and Yamada (1974) as follows:

$$\frac{De}{Dt} = -\frac{G_z g K_h}{\theta}\frac{\partial\theta_v}{\partial\sigma} + K_m\left(G_z\frac{\partial u}{\partial\sigma}\right)^2 - \frac{\alpha}{l}e^{3/2} + D_e, \tag{6}$$

where α is a constant of 0.17 and D_e represents the subgrid-scale TKE mixing and horizontal smoothing.

The model is initialized with a horizontally homogeneous uniform basic state that is hydrostatically balanced. The topography is specified using a Witch of Agnesi profile

$$h(x) = \frac{h_0 a^2}{x^2 + a^2}, \tag{7}$$

for a two-dimensional mountain of height h_0 and half-width, a, of 10 km. Simulations were conducted both with and without parameterized surface friction. We will use ''free-slip'' to describe those cases in which the turbulent vertical fluxes of horizontal momentum are set to zero at the lower boundary. Scale analysis suggests if $(h_0/a)^2 \ll 1$, this is a good approximation to the exact free-slip condition, which requires that there be no stress normal to the lower boundary. In most simulations, the vertical heat flux was also set to zero at the lower boundary, which similarly approximates the exact condition

FIG. 2. Rotor clouds and blowing dust over the Owens Valley during a mountain wave event in the lee of the Sierra Nevada (right) on 5 Mar 1950. The flow is westerly (from right to left). (Photographed by Robert Symons.)

of thermal insulation that there be no heat flux normal to the lower boundary.

In those simulations that include parameterized surface friction, which will be referred to as ''no-slip,'' the turbulent vertical fluxes of horizontal momentum between the ground and the lowest grid point are computed following the Louis (1979) and Louis et al. (1982) formulation, which makes use of Monin–Obukhov similarity theory. In the absence of the third spatial dimension and the Coriolis force, the boundary layer will gradually deepen away from the inflow boundary, without achieving a spatially homogeneous structure upstream of the mountain. To avoid introducing an artificial dependence of the boundary layer depth on the distance to the in-flow boundary, the lower boundary condition is free-slip between the inflow boundary and a point two mountain half-widths ($2a$) upstream of the mountain crest, and then linearly transitions from free-slip to fully no-slip over a horizontal distance of one mountain half-width. By using the free-slip condition over most of the distance between the mountain and the inflow boundary, it is possible to obtain highly controlled comparisons between free-slip and no-slip simulations while still capturing the regions of strongest frictional drag in the high-wind regions to the lee of the crest.

The spurious gravity waves that are generated as a result of the impulsive start in the presence of topography are diminished through a steady increase of the gravitational constant and horizontal wind profile from zero to their specified values over nondimensional time periods, t_g and t_u, such that $U(z)t_g/a = 4$ and $U(z)t_u/a = 1$, respectively, following Durran (1986) and Nance and Durran (1997). The computational domain is 259 km in length with a horizontal grid increment of 100 m for all experiments. The mountain crest is located at $12a$ or 120 km from the upstream boundary. For the two-layer experiments discussed in section 3, 110 vertical levels are used with a vertical grid increment that stretches from $\Delta z = 10$ m at the surface to $\Delta z = 100$ m at 1 km, and then remains a constant $\Delta z = 100$ m to the model top at 9.75 km. The simulations discussed in section 4 use 95 vertical levels, with $\Delta z = 10$ m at the surface, stretching to $\Delta z = 50$ m at 400 m, and then constant $\Delta z = 50$ m up to 3.4 km, stretching again to $\Delta z = 500$ m at 11.6 km, the model top. The lateral boundaries make use of the radiation condition proposed by Orlanski (1976) with the exception that the Doppler-shifted phase speed ($u \pm c$) is specified and temporally invariant at each boundary (Pearson 1974; Durran et al. 1993). Reflection of waves at the upper boundary is mitigated by a radiation condition following Klemp and Durran (1983) and Bougeault (1983).

3. Rotor dynamics in two-layer fluids

Observational evidence suggests that rotors are boundary-layer-separation phenomena that may develop in association with large-amplitude trapped lee waves. The interaction between the lee waves and the surface

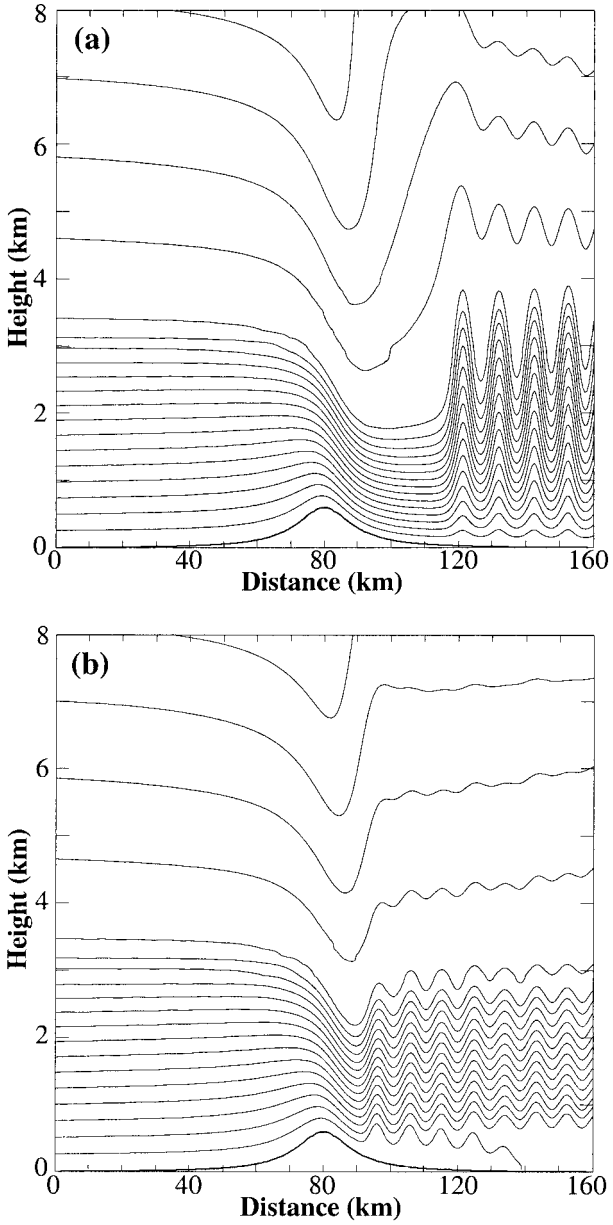

FIG. 3. Potential temperature at 3 h ($Ut/a \sim 27$) for simulations using (a) free-slip and (b) no-slip lower boundary conditions. The isentropes are plotted every 4 K. The ''mountain'' is shown as a dark line near the x axis.

boundary layer is explored in this section. To simplify the lee-wave dynamics we begin by considering atmospheric structures in which the Scorer parameter is essentially constant within each of two layers. As demonstrated by Nance (1997), the exact expression for the Scorer parameter in a compressible atmosphere (Queney et al. 1960, p. 52) is most accurately approximated as

$$l^2 = \frac{N^2}{U^2} - \frac{2\Gamma}{U}\frac{dU}{dz} - \Gamma^2 - \frac{d\Gamma}{dz} - \frac{1}{U}\frac{d^2U}{dz^2}, \qquad (8)$$

where

$$N^2 = \frac{g}{\overline{\theta}}\frac{d\overline{\theta}}{dz}, \qquad \Gamma = -\frac{N^2}{g} - \frac{1}{2\overline{\rho}}\frac{\partial\overline{\rho}}{dz},$$

and overbars denote a horizontally uniform basic state. Here ρ is density, U is the cross-mountain wind speed, g is the gravitational acceleration, and z is the vertical coordinate. The scaling assumptions required to obtain l^2 are identical to those used to obtain the pseudo-incompressible equations (Durran 1989).

We specify a particularly simple atmospheric structure in which U is a constant 25 m s^{-1} and the upper- and lower-layer Brunt–Väisälä frequencies are $N_u = 0.01$ and $N_l = 0.025$, in which case the Scorer parameters in each layer are approximately $l_u = 4 \times 10^{-4}$ m^{-1} and $l_l = 1 \times 10^{-3}$ m^{-1}. The upstream elevation of the interface between the upper and lower layers H_i is at 3 km, and the mountain height h_0 is 600 m.

The influence of surface friction on the terrain-induced perturbations is illustrated in Fig. 3, which shows isentropes of potential temperature in a 160 km wide subdomain centered on the mountain. These results are plotted at the nondimensional time $Ut/a = 27$ ($t = 3$ h), by which the solution has reached a quasi-steady state. The solution for a free-slip lower boundary is shown in Fig. 3a, whereas that in Fig. 3b shows the result for a no-slip simulation with $z_0 = 10$ cm; the surface heat flux is zero in both simulations. The free-slip solution exhibits a region of high-speed ''shooting flow'' extending over most of the lee slope and terminating in a series of large-amplitude lee waves. In contrast, the region of shooting flow terminates midway down the lee slope in the no-slip case and the amplitudes of the lee waves are significantly reduced. The wavelength of the lee waves in the no-slip case is also reduced from that in the free-slip case by about 9%. Downstream of the mountain in the no-slip case, the lowest isentrope eventually drops below the lowest level on the numerical grid (which is $\Delta z/2$ above the surface) due to diabatic mixing.

The lee-side horizontal wind speeds from these same two simulations are plotted on a smaller 60-km subdomain in Fig. 4. Surface friction acts to elevate and slightly reduce the wind speed maximum and to produce a thin shear layer just above the surface in agreement with previous downslope-windstorm simulations that incorporated surface friction (Richard et al. 1989; Miller and Durran 1991; Doyle et al. 2000). There is no reversed flow in the free-slip simulation, but in the no-slip simulation patches of reversed flow are located beneath the crests of the first two lee waves in a shallow layer less than 150 m above the surface. The rotor associated with each patch of reversed flow is approximately 3 km wide.

Neglecting compressibility, which has only a minor impact on the vorticity budget in these simulations, the y-component horizontal vorticity η is determined by the vorticity tendency equation for Boussinesq two-dimensional flow (with $f = 0$):

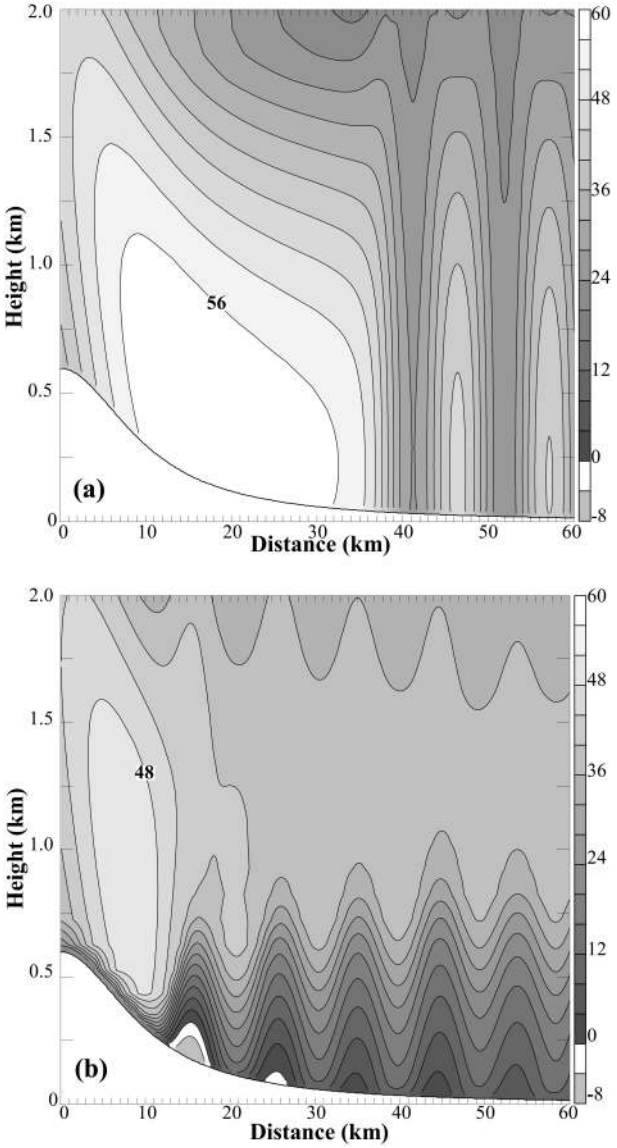

FIG. 4. Horizontal wind speed for the simulations using (a) free-slip and (b) no-slip lower boundary conditions. The isotachs are plotted every 4 m s^{-1}.

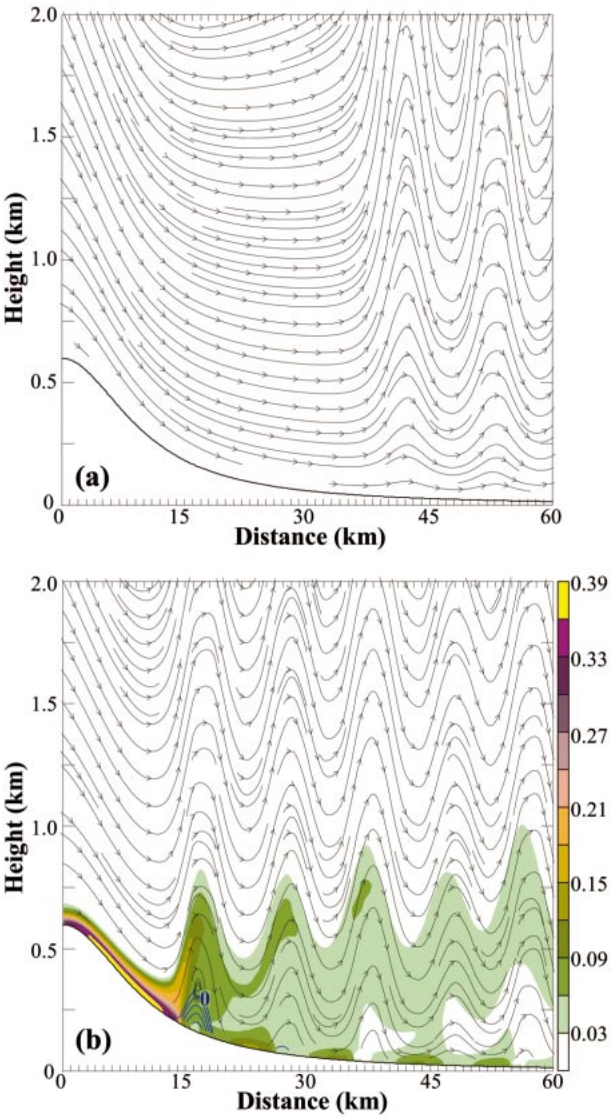

FIG. 5. Streamlines and horizontal vorticity (η) (in units of s^{-1}) for the simulations using (a) free-slip and (b) no-slip lower boundary conditions. Horizontal wind speeds less than or equal to zero are shown in (b) using blue isotachs (every 2 m s^{-1}). Horizontal vorticities greater than 0.03 s^{-1} are shaded in color. Note that η does not exceed 0.03 s^{-1} in (a).

$$\frac{D\eta}{Dt} = -\frac{\partial B}{\partial x} + \frac{\partial}{\partial z}(D_u) - \frac{\partial}{\partial x}(D_w), \tag{9}$$

in which

$$\eta = \left(\frac{\partial u}{\partial z} - \frac{\partial w}{\partial x}\right), \tag{10}$$

and the buoyancy field B given by

$$B = g\frac{\theta'}{\overline{\theta}}, \tag{11}$$

where θ' is the perturbation potential temperature. Here $\overline{\theta}$ is a fixed reference potential temperature, and $\theta' = \theta - \overline{\theta}(z)$ is the perturbation potential temperature. The first term on the right side of (9) represents the baroclinic generation of vorticity through horizontal gradients of buoyancy. The second and third terms represent vorticity sources and sinks due to subgrid-scale turbulent stresses. Note that in the two-dimensional Boussinesq limit, there is no generation of vorticity by stretching or tilting.

Streamlines are superimposed on contours of η in Fig. 5 for the same free-slip and no-slip simulations considered in Figs. 3 and 4. The 0, −2, −4, . . . horizontal velocity contours are also plotted for the no-slip simulation in Fig. 5b. (As already noted, there are no regions of stagnant or reversed flow in the free-slip sim-

ulation.) Only weak vorticity perturbations develop in the free-slip case; these perturbations are produced by baroclinic generation within the lee-wave train and are predominately negative in sign. Much stronger vorticity perturbations develop in the no-slip simulation in response to the shear stress at the lower boundary. In the no-slip case a thin sheet of high-vorticity fluid develops adjacent to the ground along the lee slope and then ascends abruptly as it is advected into the updraft at the leading edge of the first lee wave. This ascending sheet of high-vorticity air coincides with the upstream edge of the first rotor. A similar relationship is also present at the upstream edge of the second rotor, although both the vortex sheet and the strength of the reversed flow are weaker in the second rotor. The sign of the boundary layer–induced vorticity is positive, which is the same sign as the vorticity in the rotors. In the no-slip case, a vorticity maximum exceeding 0.4 s^{-1} is located immediately above the surface of the lee slope; farther aloft local maxima of approximately 0.1 s^{-1} are present in the upper portions of the first rotor near $z = 600$ m. These results support the idea that rotor formation in the no-slip simulation is associated with boundary layer separation as the low-level streamlines break away from the surface and lift vertically into the lee wave. Batchelor (1967, p. 327) noted when the ratio of the boundary layer thickness to size of a bluff body is small, boundary layer separation in high-Reynolds-number flow ''is undoubtedly associated with the empirical fact that a steady state of the boundary layer adjoining a solid boundary is impossible with an appreciable fall in the velocity of the external stream.'' In the preceding simulations, the velocity minima and pressure maxima beneath each lee-wave crest appear to provide the requisite free-stream deceleration, or equivalently a sufficient adverse pressure gradient, to induce boundary layer separation in the presence of surface friction.

The hypothesis that lee-wave-induced free-stream pressure perturbations play a important role in rotor formation by inducing boundary layer separation was tested by comparing the strength of the reversed flow in a no-slip simulation with the strength of the adverse pressure gradient in an otherwise identical free-slip simulation. Two series of comparisons were performed in which the lee-wave amplitude was systematically varied by changing either the mountain height or the atmospheric structure. The results are shown in Fig. 6, in which the magnitude of the strongest reversed rotor flow in the no-slip simulation (nondimensionalized by U) is plotted as a function of the adverse pressure gradient at the downstream edge of the shooting flow in the free-slip simulation (nondimensionalized by U^2/L). The values plotted in Fig. 6 are averages over the 30-min period centered at $t = 3$ h after the start of each simulation; these calculations are not particularly sensitive to the length of the time interval over which the average is computed.

In the first series of comparisons (plotted as diamonds in Fig. 6), pairs of free-slip and no-slip simulations were conducted for the same two-layer atmospheric structure considered in Figs. 3–5, except that the mountain height h_0 was varied over the range between 200 and 600 m. The results suggest that the strength of the lee-wave-induced adverse pressure gradient at the edge of the shooting flow in the *free-slip* simulation is strongly correlated with the strength of the reversed flow in the *no-slip* simulations. No reversed flow appears until the mountain height exceeds a threshold between 300 and 400 m; further increases in the mountain height induce stronger lee waves, larger adverse pressure gradients, and stronger rotors.

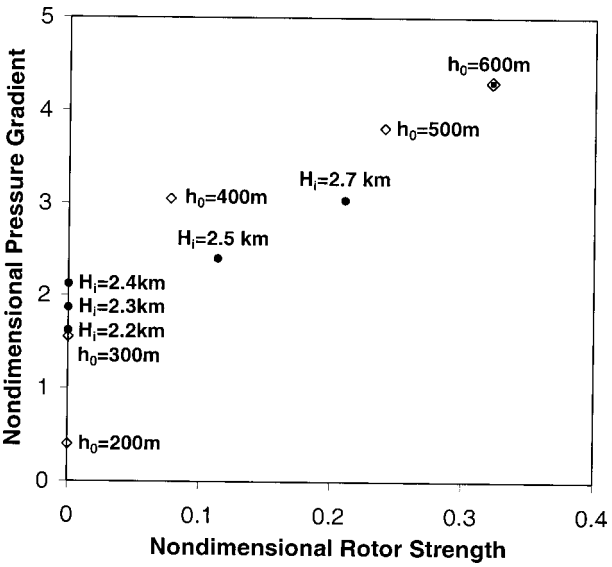

FIG. 6. Regime diagram summarizing the simulations performed with varying mountain height (h_0) and interface depth (H_i) as a function of rotor strength (nondimensionalized by U) and pressure gradient (nondimensionalized by U^2/L).

In the second series of comparisons (plotted as circles in Fig. 6), the mountain height is fixed at $h_0 = 600$ m and the lee-wave amplitude is modulated by varying the height of the interface H_i between the upper and lower layers. When the interface is at or below 2.4 km, the waves are too weak to induce rotors. As H_i increases the lee waves become stronger, the lee-wave-induced adverse pressure gradients in the free-slip simulation increase, and the rotors become stronger in the corresponding no-slip simulations. Both sets of numerical experiments (varying h_0 with H_i fixed, varying H_i with h_0 fixed) yield similar results, although the results do not collapse onto a single curve. It is not particularly surprising that these results do not collapse onto a single curve because the depth of the lower layer is likely to exert an additional direct influence on the strength of the rotors. Nevertheless, it is interesting that both sets of experiments suggest that a minimum adverse pressure gradient (with a normalized value of about 2.2) is required as a threshold for rotor formation. It should be

noted that the minimum adverse pressure gradient required for rotor development may be dependent on other factors, such as the terrain shape, so the nondimensional value of 2.2 should not be interpreted as a universal constant.

As h_0 is increased in the simulations in Fig. 6, the increase in rotor strength is also accompanied by an increase in the intensity of the downslope winds and the *y*-component vorticity in the boundary layer along the lee slope. Thus, one might hypothesize that in the free-slip simulations it is actually the strength of the downslope winds (or equivalently the *y*-component vorticity), rather than the lee-wave amplitude, that most strongly correlates with the rotor intensity in the no-slip simulations. This hypothesis can be discounted by noting that in the other series of simulations shown in Fig. 6, in which h_0 is fixed and H_i varies, the maximum downslope wind speeds in the free-slip simulations are almost independent of the interface depth. In particular, as H_i increases and the rotors in the no-slip simulations intensify, the increase in the downslope wind speed in the corresponding series of free-slip simulations is much smaller than the increase in the lee-wave-induced pressure gradient. For example, as H_i increases from 2.5 to 3.0 km, the strength of the reversed flow in the no-slip simulations increases by a factor of three, while in the free-slip simulations the percentage increase in the lee-wave-induced pressure gradient is roughly four times as large as the percentage increase in the maximum downslope wind speed.

Further indication of the important role played by lee waves in facilitating rotor formation is illustrated by the pair of no-slip simulations shown in Fig. 7. The upstream profile of potential temperature has the same two-layer structure used in the previous simulations shown in Figs. 3–5, and the mountain height is once again set to 600 m; however, the mean wind speed now decreases linearly from 25 to 10 m s^{-1} throughout an elevated shear layer. As a consequence of this wind shear, the Scorer parameter above the shear layer increases to approximately 1×10^{-3} m^{-1}, which is the same as the value of l_l, thereby creating a mean state that will not support completely trapped lee waves. In the first simulation shown at $t = 3$ h in Fig. 7a, the mean-state shear is located in the layer between 4 and 7 km, and the upstream flow supports partially trapped lee waves. The streamlines for this case, plotted at $t = 3$ h in Fig. 7a, show rotors forming beneath the crest of the first four lee waves downstream from the crest. The reversed flow in the first rotor exceeds 17 m s^{-1}. The *y*-component vorticity, also plotted in Fig. 7a, shows a sheet of high-vorticity fluid developing in response to surface friction along lee slope and then lifting upward into the first lee wave in a manner similar to that in Fig. 5b.

In the second simulation the mean-state shear is confined to a lower layer between 2 and 4 km. This atmospheric profile is much less favorable for the development of partially trapped lee waves. The streamlines for this case, plotted in Fig. 7b, show a weak poorly defined train of lee waves without any rotors. Nevertheless the downslope winds in this case are very strong; the maximum speed exceeds 60 m s^{-1}, which is 20% stronger than the maximum leeside wind speed for the case with rotors (Fig. 7a). The stronger leeside winds generate higher values of *y*-component vorticity at the base of the shooting flow along the lee slope. The intensification of η, relative to that shown in Fig. 7a, appears to produce a mild instability in which the thickness of the vortex sheet at the lower boundary in Fig. 7b develops a series of undulations. Note, however, that rotors and reversed flow never develop as a consequence of these undulations. The simulations shown in Fig. 7

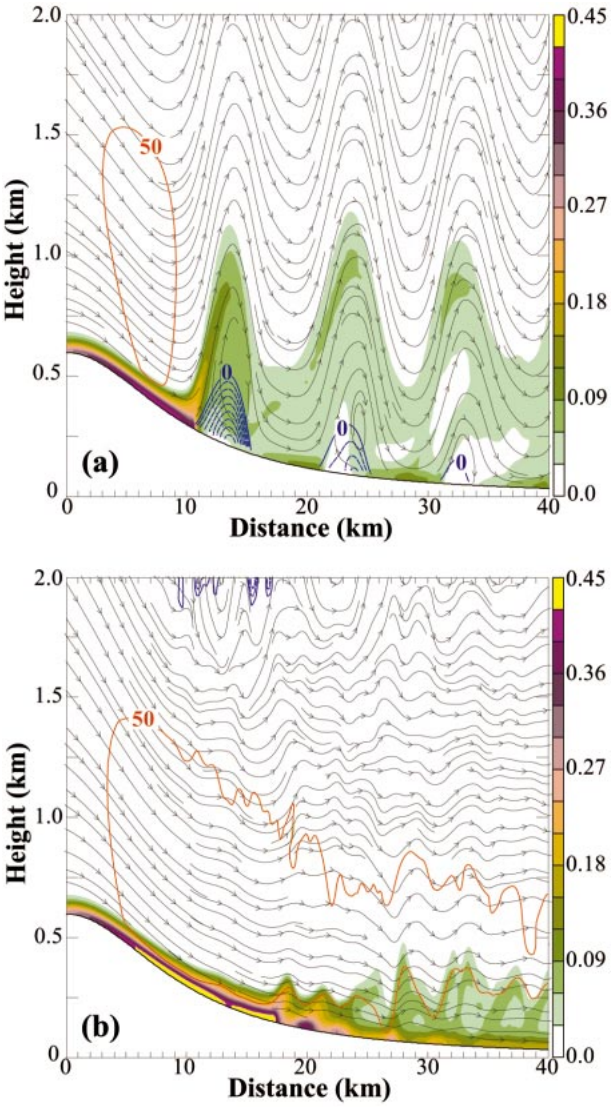

FIG. 7. Streamlines and horizontal vorticity (η) for the simulations with vertical shear confined to the (a) 4–7-km and (b) 2–4-km layers. Horizontal wind speeds less than or equal to zero are shown using blue isotachs (every 2 m s^{-1}) and the 50 m s^{-1} isotach is shown in red. Horizontal vorticities greater than 0.03 s^{-1} are shaded in color.

demonstrate that in the absence of significant lee-wave activity, rotors need not develop even when the downslope winds are very high, but on the other hand, large-amplitude lee waves can produce very strong rotors even when the downslope winds are relatively modest.

The baroclinic generation of vorticity may be large enough under some circumstances to lead to rotor development even with a free-slip lower boundary condition. One example of this type is provided by the computations of Long (1955) for the steady flow of large-amplitude lee waves in a stratified fluid bounded above and below by a rigid lid. Long's analysis applies to flows in which the upstream values of N and U are constant; the lee waves are not trapped by vertical variations in the Scorer parameter, but rather by the rigid upper boundary. Can rotors also be produced without surface friction in atmospheric structures of the type considered in this section? To answer this question we conducted a series of free-slip simulations using constant values for U and a variety of two-layer static-stability profiles. The nonlinear wave trains that developed in these simulations typically became very nonsteady and generated regions of wave breaking and reversed flow aloft without producing low-level circulations resembling classical rotors.

A low-level rotor was, nevertheless, generated in one free-slip simulation in which $U = 10$ m s^{-1}, $N_l = 0.01$ s^{-1}, $N_u = 0.00387$ s^{-1}, and $H_i = 3$ km. The mountain was specified by the Witch of Agnesi profile (7) with $h_0 = 900$ m and $a = 3$ km. This simulation is identical to the ''DJT'' case in Nance and Durran (1998), except that the mountain height has been increased to 900 m from 385 m. Nance and Durran found that this atmospheric structure was relatively resistant to the development of nonstationary lee-wave perturbations through nonlinear wave interactions. The streamlines for this free-slip case are displayed at $t = 4$ h in Fig. 8a, together with contours for the reversed portion of the horizontal velocity field. A rotor is evident beneath the first lee wave with reversed flow extending up to 2 km. The maximum reversed flow is $\sim$2.8 m s^{-1} and is located over 1 km above the surface. The rotors in this simulation are nonstationary and tend to propagate upstream, as indicated by the contour plot of surface horizontal wind speed as a function of x and t in Fig. 9a. The transients in the free-slip case appear similar to those examined in Nance and Durran (1998), who concluded that they are generated by nonlinear wave interactions.

If the preceding simulation is repeated with the surface boundary layer parameterization activated, the lee waves become much weaker yet the maximum reversed flow in the rotors increases by 50% (to 4.5 m s^{-1}) (cf. Figs. 8a,b). Evidently the vorticity production in the boundary layer in the no-slip simulation more than compensates for the decrease in baroclinic vorticity production in the lee waves. In comparison with those in the free-slip case, the rotors in the no-slip simulation are also much shallower, much steadier (cf. Figs. 9a,b),

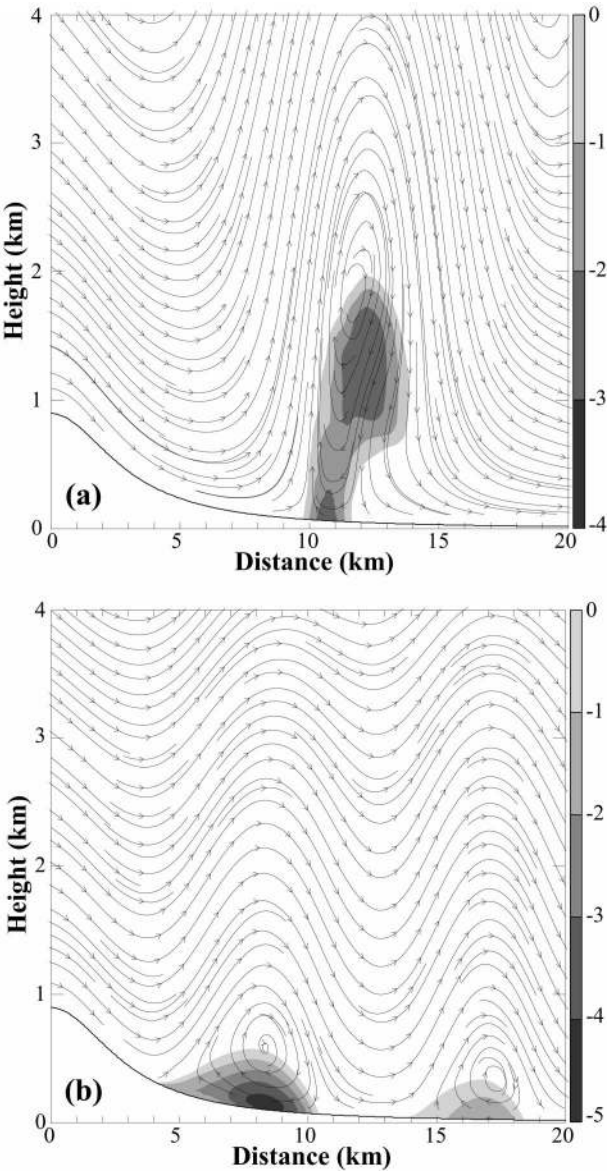

FIG. 8. Streamlines and horizontal wind speed (m s^{-1}) for the simulations using (a) free-slip and (b) no-slip lower boundary conditions for the case with l_l^2 is 1×10^{-6} m^{-1} and l_u^2 is 1.5×10^{-7} m^{-1}. Horizontal wind speed contours less than zero are shaded.

and qualitatively more similar to the observed rotor circulation presented in Fig. 1.

It is interesting to note that the role of surface friction in promoting boundary layer separation and rotors is also evident in the classical laboratory experiments of Long (1955). Figure 10, which is reproduced from Long (1955), shows a comparison of a laboratory experiment and a theoretical calculation for approximately the same flow. The theoretical calculation is based on Long's equation with free-slip rigid upper and lower boundaries. In the laboratory experiment an obstacle was towed along the bottom of a tank of stratified saltwater, and the top of fluid formed a free surface. Long's the-

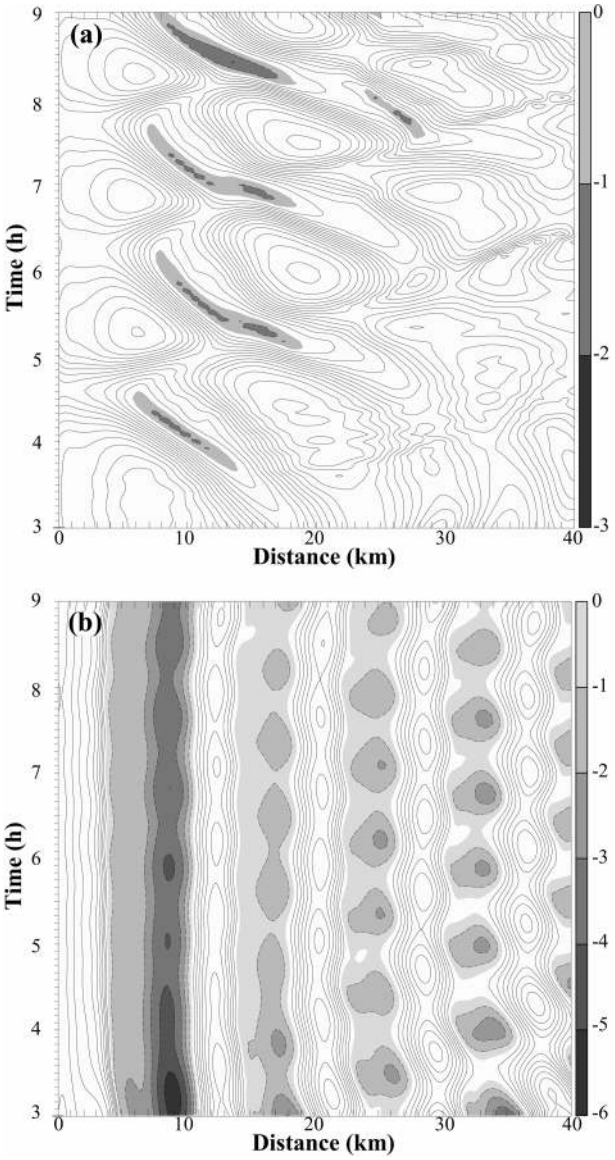

FIG. 9. Horizontal wind speed at the surface in the x–t plane for the simulations using (a) free-slip and (b) no-slip lower boundary conditions for the cases shown in Fig. 8. Regions of reversed wind flow at the surface are shaded. The isotach intervals are (a) 1 m s^{-1} and (b) 2 m s^{-1}. The zero contour is suppressed.

oretical calculations do not predict stagnation or flow reversal at any point in the fluid, yet the laboratory model shows a region of stagnant or possibly reversed flow adjacent to the lower boundary beneath the first lee wave (the cloudy white region under the first crest). Long attributes the development of this region to boundary layer separation and states that ''the fluid in the boundary layer is then carried into the body of the fluid to form a large turbulent eddy.'' As evident in Figs. 8 and 9 of Long (1955), there are other conditions under which rotor formation is both observed in the laboratory and predicted by theoretical calculations for flow with free-slip rigid upper and lower boundaries. On the other hand, very large-amplitude solutions to Long's equation for (nonhydrostatic) free-slip flows in which the rigid lid is replaced by an open upper boundary do not exhibit rotors or any significant low-level lee-wave activity (Laprise and Peltier 1989, Fig. 4). These classical tank experiments and theoretical solutions to Long's equation reinforce our finding that boundary processes and lee-wave-induced perturbations interact synergistically to facilitate the formation of rotors.

4. Sensitivity to surface momentum and heat flux

The simulations discussed in the previous section have demonstrated the importance of boundary layer processes in the development of realistic atmospheric rotors. In this section we examine the sensitivity of the rotor circulation to variations in the surface stress and the heat flux through the lower boundary. These sensitivity tests will be conducted using an upstream reference state representative of the conditions under which rotors form in the real atmosphere; in particular we will consider a vertical profile approximating the conditions upstream of the Colorado Front Range on 1200 UTC 3 March 1991. This is a few hours before a B-737 crashed at the Colorado Springs, Colorado, airport; however, since the topography in the immediate vicinity of Colorado Springs is highly three-dimensional, these two-dimensional simulations should not be interpreted as giving approximations of the airflow at the location of the plane crash. These simulations are more representative of the flow present a little farther north where the upstream topography is more nearly two-dimensional. Indeed the presence of rotor clouds was noted in the hourly observations reported by the U.S. Air Force Academy between 1355 and 1555 UTC on 3 March 1991.

The sounding used in these simulations, which is shown in Fig. 11, is a blend of the potential temperature and cross-mountain wind component observed in the Grand Junction, Colorado; Denver, Colorado; and Lander, Wyoming, soundings at 1200 UTC 3 March 1991. For the purposes of defining the mean surface pressure, the surface elevation far away from the ridge was specified as 1.5 km above mean sea level. As evident in Fig. 11, the potential temperature profile is characterized by weak static stability near the surface, capped by an inversion in the 2800–3300-m layer. The cross-mountain wind component throughout the troposphere increases from roughly 5 m s^{-1} at the surface to 45 m s^{-1} near the top of the domain. The mountain height used in the simulations is 1500 m, which is roughly representative of the mean elevation gain between the eastern plains and the crest of the Colorado Front Range. The Front Range is asymmetric with the lee slopes steeper than the upwind slopes. To represent this asymmetry, a two-sided Witch of Agnesi profile is used in the simulations

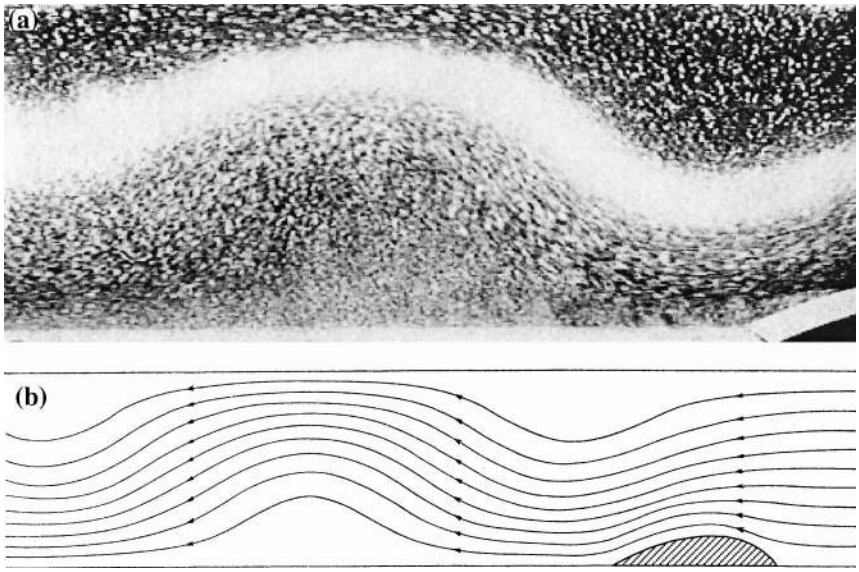

FIG. 10. (a) Stratified fluid tank experiment results and (b) finite-amplitude solution for a Froude number in the $(2\pi)^{-1}$ to π^{-1} range (from Long 1955).

with an upwind half-width of 20 km and a downwind half-width of 10 km.

First consider a control simulation in which the surface roughness length z_0 is 0.1 m and there is no surface heating. The flow 3 h into the control simulation (at which time a quasi-steady state has been attained) is indicated by the streamlines, isotachs, and contours of *y*-component vorticity plotted in Fig. 12. Trapped lee waves are clearly apparent in the streamline field with trough to crest amplitudes exceeding 1200 m. Significant downslope winds, with a maximum of approximately 25 m s^{-1}, develop along the lee slope. Regions of reversed surface wind speeds associated with the rotors are also present beneath the crests of the first three waves. The first rotor downstream of the ridgeline is the strongest, with a maximum reversed wind speed of 6.0 m s^{-1} and a region of recirculating fluid extending above the mountain crest. A vortex sheet originates in the region of high shear within the boundary layer along the lee slope and then separates from the surface and ascends into the crest of the first lee wave in a manner similar to that in the two-layer cases presented previously (cf. Figs. 5b and 7a). This well-defined layer of high-vorticity air remains aloft as it is advected downstream by the undulating flow in the lee waves. Consistent with the two-layer results presented in the previous section, an otherwise identical simulation with a free-slip lower boundary condition (not shown) does not develop rotors or reversed flow.

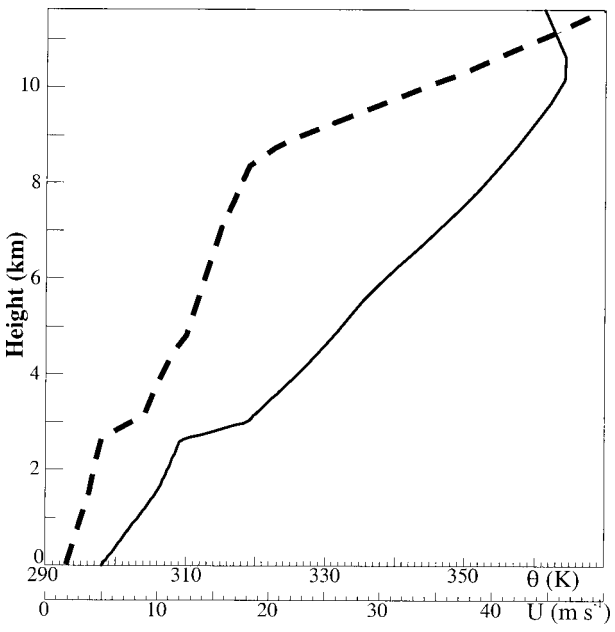

FIG. 11. Profiles of potential temperature (K) (dashed) and cross-mountain wind speed (m s^{-1}) (solid) for the Colorado Springs, CO, lee-wave case. The upstream conditions were determined from the Grand Junction, CO; Denver, CO; and Lander, WY, soundings at 1200 UTC 3 Mar 1991. The height shown is above ground level.

The influence of variations in the surface stress on the rotors is investigated through a series of simulations in which the surface roughness length is increased from 10^{-4} m, corresponding to smooth ice, to 10 m, which is typical of forests or cities (e.g., Panofsky and Dutton 1984). Note that the vertical structure of the flow arriving at the base of the windward slope is essentially independent of the value of z_0 because, as discussed in section 2, a free-slip lower boundary condition is imposed throughout the region extending from the upstream lateral boundary to a distance $2a$ upstream of the mountain crest.

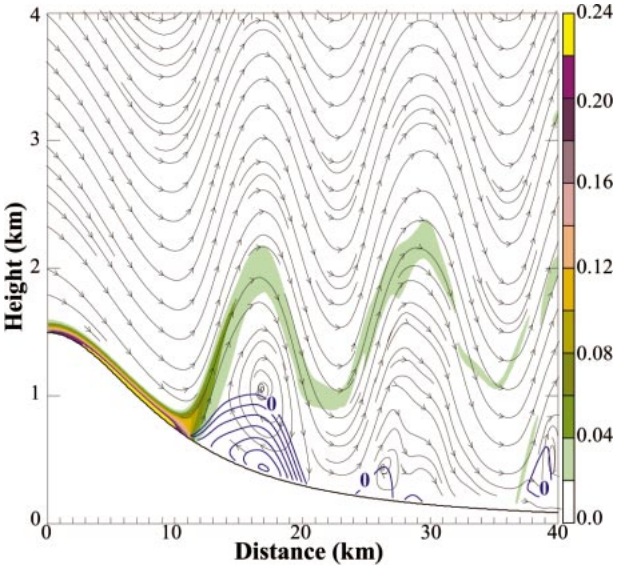

FIG. 12. Streamlines and horizontal vorticity (η) for the Colorado Springs case using a no-slip lower-boundary condition. Horizontal wind speeds less than or equal to zero are shown using blue isotachs (every 1 m s^{-1}). Horizontal vorticities greater than 0.02 s^{-1} are shaded in color.

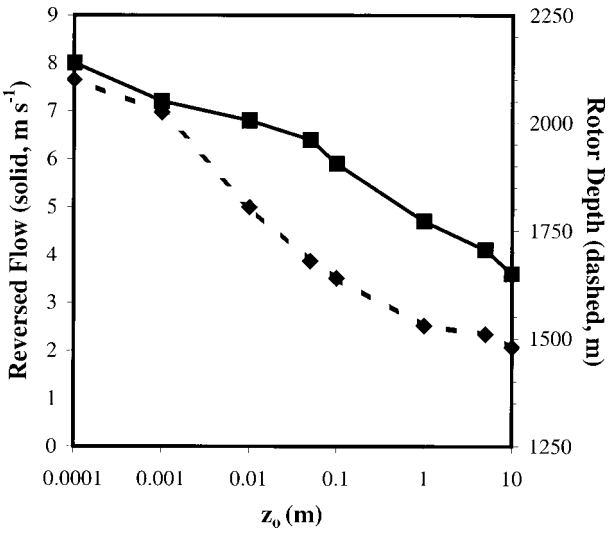

FIG. 13. Strength of the reversed rotor flow (solid line, m s^{-1}) and rotor depth (dashed line, m) plotted as a function of surface roughness length.

Results from these simulations at time $t = 3$ h are presented in Fig. 13, which shows the strength of the reversed flow in the first rotor and the depth of the rotor circulation as measured by the maximum height above the underlying topography to which the sheet of high-vorticity air ascends in the first lee-wave crest. The focus is on the first rotor because it is the most intense. As the surface roughness increases from 10^{-4} to 10 m the strength of the reversed flow decreases by 50% and the depth of the rotor decreases by 30%. Although the rotors intensify as z_0 decreases, no rotors form in the corresponding free-slip flow. This parametric dependence of the overall flow structure on z_0 is common to many types of boundary layer separation phenomena in which separation persists in the limit of vanishing viscosity, so that the flow fails to approach the free-slip solution (e.g., Batchelor 1967).

The rotors weaken as surface roughness is increased because the rotor strength is primarily influenced by the lee-wave amplitude rather than the magnitude of the boundary layer vorticity. For example, as z_0 increases from 10^{-4} to 10 m, the maximum y-component vorticity in the boundary layer more than doubles and yet the rotors weaken. This increase in η (or equivalently, this increase in the vertical shear of the horizontal wind) occurs even though the increase in z_0 produces a thicker boundary layer and a modest reduction in the maximum downslope winds at the top of the boundary layer, because as z_0 increases the dominant influence on η within the boundary layer arises from the decrease in the horizontal wind speed at the lowest grid level. As was the case for the pair of simulations shown in Fig. 7, the results from this series of simulations suggest that increases in the strength of the boundary-generated vorticity do not necessarily lead to stronger rotors. The actual strength of the rotor is once again a strong function of the lee-wave amplitude, which (as indicated by the decrease in the depth of the rotor) decreases as z_0 increases. The decrease in lee-wave amplitude with increasing z_0 may be understood, in a holistic sense, as the consequence of viscous dissipation in the boundary layer reducing the magnitude of the energy flux that must be carried downstream by the lee waves.

Increases in z_0 also lead to a reduction in the cross-mountain pressure drag D,

$$D = \int_{-\infty}^{+\infty} p_s \frac{\partial h}{\partial x}\, dx,$$

as indicated in Fig. 14, where p_s is the surface pressure. Also plotted in Fig. 14 is the distance downstream from the crest at which the boundary layer separates from the surface and rises into the first lee wave. Clearly, the variations in cross-mountain pressure drag are closely related to the variations in the downstream distance at which the boundary layer separates from the surface. As surface friction increases, the boundary layer separates earlier and the minimum in the leeside pressure perturbation is not as spatially extensive, which results in an overall reduction in the drag. Also, increasing z_0 reduces slightly the magnitude of the leeside pressure perturbations throughout the region upstream of the separation point, although, as suggested by the high correlation between the two curves shown in Fig. 14, this has only a minor influence on the total cross-mountain pressure drag. Our basic result, that increasing the surface roughness decreases the pressure drag, is consistent with results previously obtained by Richard et al. (1989)

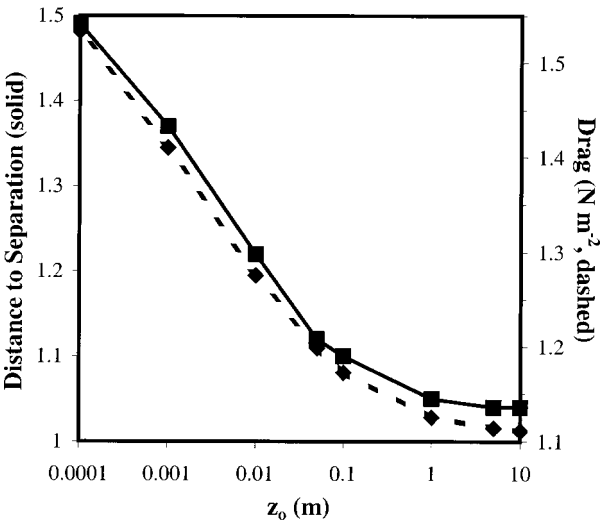

FIG. 14. Distance to separation (solid, nondimensional) and pressure drag D (dashed, N m^{-2}) as a function of surface roughness length. The distance to separation is defined as the distance downstream from the crest at which the boundary layer separates from the surface and is nondimensionalized by the mountain half-width.

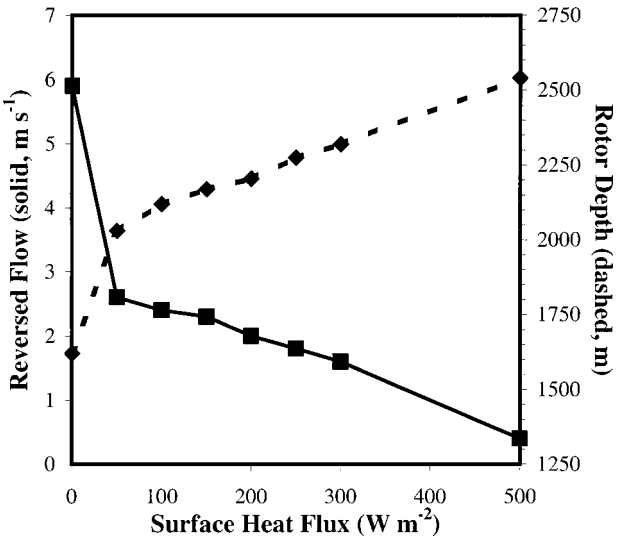

FIG. 15. Strength of the reversed rotor flow (solid line, m s^{-1}) and rotor depth (dashed line, m) as a function of surface heat flux (W m^{-2}).

and Ólafsson and Bougeault (1997). Although these authors conducted hydrostatic simulations that did not generate rotors, their calculations did show the same tendency for reductions in z_0 to allow the primary wave trough to penetrate farther down the lee slope and thereby increase the cross-mountain pressure drag.

There is a superficial similarity between the decrease in the pressure drag on the mountain as z_0 is increased and the decrease in aerodynamic drag on a golf ball created by roughening the surface of the ball—in both cases the increase in surface roughness reduces drag by changing the location at which the boundary layer separates from the surface. The detailed behavior in each case is, however, completely opposite. There would be no drag on a golf ball traveling through a homogeneous fluid if the flow were completely inviscid and remained attached to the entire surface of the ball. Roughening the surface of the golf ball moves the point of boundary layer separation *downstream* of that which would occur in flow over a smooth ball and thereby reduces the aerodynamic drag. On the other hand, when buoyancy forces produce gravity waves in stably stratified flow over a mountain, the cross-mountain pressure drag is greatest when the leeside pressure trough extends the maximum distance downstream. Roughening the boundary layer moves the point of boundary layer separation *upstream* thereby reducing the spatial extent of the leeside pressure anomaly and the pressure drag.

In many mountain-wave events there is a pronounced asymmetry in the solar radiation reaching the ground because a foehn cloud is present upstream while much of the lee slope is cloud free. Measurements taken during the Sierra Wave Project showed that the air passing through the crests of rotor clouds in the lee of the Sierra extended to a higher altitude than its initial position in the upstream flow. Some extension of the air parcels above their levels upstream is simply the consequence of the nonhydrostatic accelerations in the lee waves themselves. Nevertheless, Kuettner (1959) hypothesized that solar insolation along the lee slope might also play an important role in increasing the depth of the rotor circulations. Kuettner noted that surface heating reduces the depth-integrated static stability in the lowest layer of the fluid, and that in the context of hydraulic theory, this can be modeled as a decrease in the density jump at the top of the shallow-water layer. Kuettner's shallow-water computations confirmed that a decrease in the gravitational restoring force across the free surface downstream of the obstacle crest could lead to significantly higher hydraulic jumps.

Motivated by Kuettner's results, we conducted a second series of experiments to investigate the effect of leeside surface heat fluxes on the rotors. Surface heat fluxes of 50, 100, 150, 200, 250, 300, and 500 W m^{-2} were imposed throughout the half-domain downstream from the mountain crest. These experiments all were conducted with $z_0 = 0.1$ m and used the composite Colorado Springs sounding shown in Fig. 11. The results from this series of simulations are summarized in Fig. 15, in which the strength of the reversed flow and the depth of the rotor circulation at $t = 3$ h are plotted as a function of the surface heat flux. As in Fig. 13, the depth of the rotor circulation is measured by the maximum height above the underlying topography to which the sheet of high-vorticity air ascends in the first lee-wave crest. Even with relatively weak surface heating of 50 W m^{-2}, the strength of the reversed flow decreases by more than 50% and the depth of the circulation nearly doubles relative to the values for the simulation with

no heating. Further incremental increases in the surface heat flux lead to a nearly linear decrease in the strength of the reversed flow and a nearly linear increase in the rotor depth. When the surface heat flux is 300 W m^{-2}, the reversed flow is less than 2 m s^{-1} and the top of the rotor circulation extends to 2300 m above the surface (to $z = 2800$ m). The direct relationship between increases in the surface heat flux and the rotor depth shown in Fig. 15 is in qualitative agreement with Kuettner's results. These results also agree with pilot reports from the Sierra Wave Project, which indicated that rotor clouds typically reached their greatest heights in the late afternoon (Kuettner 1959).

An alternative explanation for the increase in lee-wave amplitude in response to surface heating is provided by linear theory. As noted by Corby and Wallington (1956), the amplitude of a linear lee wave typically increases if the atmospheric structure is pushed closer to the critical condition beyond which no resonant waves can be supported. In particular, suppose that a two-layer atmosphere will support resonant waves for either of two values of the Brunt–Väisälä frequency in the lowest layer N_l, while all other factors, such as the upper-level stability, the interface height, and the cross-mountain wind speed, remain the same. Then, as demonstrated in Fig. 3 of Corby and Wallington, the largest amplitude lee waves will occur in the case with the smaller N_l. Since the net effect of the surface heating in the preceding simulations is to reduce the average static stability throughout the layer between the ground and the inversion at 2.7 km above ground level, the results of Corby and Wallington suggest that surface heating should produce larger amplitude lee waves (at least until the heating becomes so strong that it untraps the waves).

The surface heat flux also exerts an important influence of the intensity of the turbulence within the rotor. In these simulations, the turbulence is most closely related to the field of subgrid-scale kinetic energy, TKE, governed by (6). The TKE field for the case with no surface heating is compared with that for a surface heat flux of 300 W m^{-2} in Fig. 16. Shear production is the dominant source of TKE in the simulation without surface heating (Fig. 16a), in which the maximum value of TKE is 12.7 m^2 s^{-2}. Buoyancy production significantly increases both the maximum intensity and the total domain averaged TKE when the surface heat flux is nontrivial. The maximum TKE for the experiment with a modest surface heat flux of 50 W m^{-2} increases to 15.2 m^2 s^{-2}. When the heat flux is 300 W m^{-2}, the maximum TKE is 16.8 m^2 s^{-2}, and as shown in Fig. 16b, the spatial extent of the turbulent region is much larger.

In both cases shown in Fig. 16, a distinct plume of TKE extends from the surface to the top of the rotor along the upstream edge of the first lee wave. This spatial distribution of the TKE within the rotor is in good agreement with the observations of Lester and Fingerhut

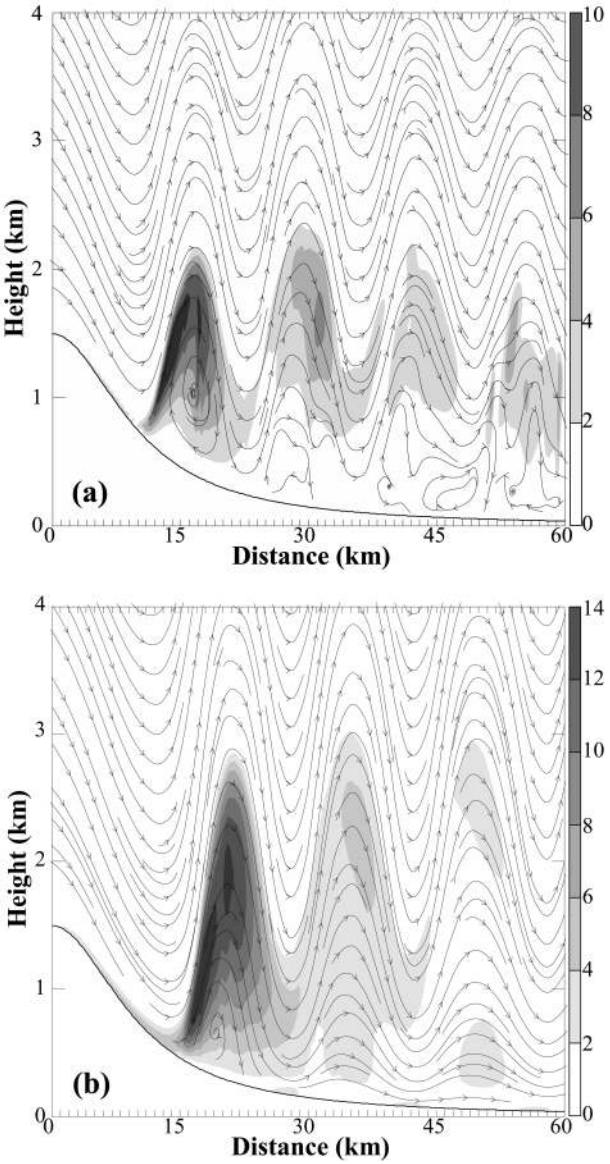

FIG. 16. Turbulent kinetic energy (grayscale m^2 s^{-2}) and streamlines for the no-slip simulations with (a) no surface heating and (b) 300 W m^{-2} heat flux. The shading interval for the TKE is 2 m^2 s^{-2}.

(1974), who conducted several flights through rotors in the lee of the Rockies and concluded that ''the most common feature of the turbulence fields for all cases was the occurrence of severe turbulence in the updraft area just upstream of the rotor.'' The actual values of $\overline{u'^2}$reported in Lester and Fingerhut as characteristic of extreme turbulence are roughly 2.5 m^2 s^{-2}, which are considerably weaker than the maximum TKE values of roughly 13 m^2 s^{-2} obtained in these simulations. The lack of better quantitative agreement between these simulations and the aircraft data is not, however, particularly significant since the TKE computed in the simulations also includes the contribution from the variance of the vertical velocity $\overline{w'^2}$ and because the averaging intervals

used to define perturbations and compute averages in the observations are very different from those in the simulations. Magnitudes of TKE similar to those shown in Fig. 16 were reported by Dawson and Marwitz (1982) from an analysis of low-level aircraft measurements in the updraft of a hydraulic jump downwind of Windy Gap, Wyoming. Smith (1987) reported values of TKE computed from aircraft data collected in the Croatian bora that are an order of magnitude larger than those in this simulation: values of $(\overline{u'^2} + \overline{w'^2})/2$ on the order of 250 $m^2\ s^{-2}$ may be deduced from the entries in his Table 2. Smith also notes that his results are very sensitive to the length of the record used in the computation of the velocity variance, with maximum values of $\overline{w'^2}$ dropping by an order of magnitude when the record length is increased from 10 to 100 s. We conclude that the values of TKE obtained in our simulations lie within the range of turbulence intensities actually observed in the vicinity of low-level rotors and hydraulic jumps.

5. Summary and conclusions

We have investigated the dynamics of mountain-wave-induced rotors through a series of high-resolution two-dimensional simulations with the nonhydrostatic COAMPS model. Our results demonstrate that surface–boundary layer drag and the development of adverse pressure perturbations in trapped mountain lee waves act in a synergistic manner to facilitate the formation of low-level rotors. Surface friction creates a layer of strong vertical shear, or equivalently a layer of high *y*-component vorticity in the downslope winds to the lee of the crest. This layer of high-vorticity air separates from the surface in a region of adverse pressure gradient associated with the first lee wave downstream from the ridge line. After lifting off the surface, the vortex sheet is advected upward into the crest of the first lee wave. A significant fraction of this vorticity is subsequently advected downstream through the lee-wave train, but a portion is captured in the region below the wave crest and contributes to the formation of a rotor whose *y*-component vorticity has the same sign as that generated within the boundary layer along the lee slope.

A series of simulations was performed in which the upstream static stability was constant within each of two layers. These simulations showed that the magnitude of the reversed flow with the primary rotor in a no-slip simulation was highly correlated with the strength of the adverse pressure gradient in the primary lee wave in an otherwise identical free-slip simulation. Even in the no-slip simulations, rotors did not form unless the adverse pressure gradient in the corresponding free-slip simulation exceeded a threshold value of about 2.2 nondimensional units. An additional pair of simulations demonstrated that an atmospheric reference state unfavorable for the development of lee waves can sustain higher values of boundary layer vorticity without forming rotors than can a second reference state more favorable for lee-wave development. Finally, other simulations suggest it is relatively difficult to form rotors with a free-slip lower boundary, and even in the one free-slip case we did identify that produces reversed rotor flow, the rotors that form in the corresponding no-slip case are much steadier and more robust. The finding that surface friction favors the development of rotors in flows with resonant lee waves is consistent with the comparison of laboratory and theoretical models presented by Long (1955).

In addition to the two-layer simulations, we conducted two more sets of numerical experiments using an upstream sounding characteristic of that which produced rotor clouds near the U.S. Air Force Academy in Colorado on 3 March 1991. The first set of experiments demonstrated that increases in surface roughness beyond the smallest nonzero value considered in these simulations (10^{-4} m) weakens the reversed flow and decreases the depth of the rotor. Nevertheless, since no rotors form in the free-slip case, the free-slip simulation does not serve as a lower bound to which the no-slip simulations asymptote as the surface roughness approaches zero. Increasing the surface roughness also decreased the cross-mountain pressure drag, primarily by shifting the point of boundary layer separation upstream and thereby reducing the extent of the leeside pressure anomaly.

The influence of leeside surface heat fluxes was investigated in the second set of numerical experiments performed with the Colorado sounding. Increasing the surface heat flux decreased the strength of the reversed rotor flow, but in agreement with the hypothesis of Kuettner (1959), increasing the heat flux did increase the depth of the rotor circulation. In addition, surface heating intensified the plume of subgrid-scale turbulent kinetic energy extending along the upwind side of the first lee wave from the surface to the wave crest. The distributions of the patches of most intense turbulence within the rotors in these simulations are consistent with pilot reports from a variety of observational programs and in particular with the aircraft data analyzed by Lester and Fingerhut (1974).

The two-dimensional framework used in this study precludes vorticity generation by stretching or tilting. Vortex stretching and tilting are likely to play an important role in the dynamics of small-scale subvortices within the parent rotor. These subrotors, which are analogous to multiple suction vortices within a tornado, appear to pose the greatest hazard to aviation and are the subject of continuing study.

Acknowledgments. The research support for the first author was provided by the Office of Naval Research (ONR) Program Element 0601153N. The support for the second author was provided by the National Science Foundation Grant ATM-9817728. We gratefully acknowledge Joachim Kuettner for helpful discussions concerning his observational experience with mountain-

induced rotor flows. We also thank Ronald B. Smith and Richard Rotunno for beneficial discussions. Computing time was supported in part by a grant of HPC time from the Department of Defense Shared Resource Center, Stennis Space Center, Mississippi, and performed on a Cray T-90.

REFERENCES

Batchelor, G. K., 1967: *An Introduction to Fluid Mechanics.* Cambridge Press, 615 pp.

Bougeault, P., 1983: A non-reflective upper boundary condition for limited-height hydrostatic models. *Mon. Wea. Rev.,* **111,** 420–429.

Clark, T. L., W. D. Hall, R. M. Kerr, D. Middleton, L. Radke, F. M. Ralph, P. J. Neiman, and D. Levinson, 2000: Origins of aircraft-damaging clear-air turbulence during the 9 December 1992 Colorado downslope windstorm: Numerical simulations and comparison with observations. *J. Atmos. Sci.,* **57,** 1105–1131.

Corby, G. A., and C. E. Wallington, 1956: Airflow over mountains: The lee-wave amplitude. *Quart. J. Roy. Meteor. Soc.,* **82,** 266–274.

Dawson, P. J., and J. D. Marwitz, 1982: Wave structures and turbulent features of the winter airflow in southern Wyoming. Geological Society of America, Special Paper 192, 55–63.

Doyle, J. D., and Coauthors, 2000: An intercomparison of model-predicted wave breaking for the 11 January 1972 Boulder windstorm. *Mon. Wea. Rev.,* **128,** 901–914.

Durran, D. R., 1986: Another look at downslope windstorms. Part I: The development of analogs to supercritical flow in an infinitely deep, continuously stratified fluid. *J. Atmos. Sci.,* **43,** 2527–2543.

——, 1989: Improving the anelastic approximation. *J. Atmos. Sci.,* **46,** 1453–1461.

——, and J. B. Klemp, 1983: A compressible model for the simulation of moist mountain waves. *Mon. Wea. Rev.,* **111,** 2341–2361.

——, M. Yang, D. N. Slinn, and R. G. Brown, 1993: Toward more accurate wave permeable boundary conditions. *Mon. Wea. Rev.,* **121,** 604–620.

Hodur, R. M., 1997: The Naval Research Laboratory's Coupled Ocean/Atmosphere Mesoscale Prediction System (COAMPS). *Mon. Wea. Rev.,* **125,** 1414–1430.

Holmboe, J., and H. Klieforth, 1957: Investigations of mountain lee waves and airflow over the Sierra Nevada. Final Rep. Contract AF19(604)-728, University of California ADNo. 133606, Department of Meteorology, University of California, Los Angeles, 290 pp.

Klemp, J., and R. Wilhelmson, 1978: The simulation of three-dimensional convective storm dynamics. *J. Atmos. Sci.,* **35,** 1070–1096.

——, and D. R. Durran, 1983: An upper boundary condition permitting internal gravity wave radiation in numerical mesoscale models. *Mon. Wea. Rev.,* **111,** 430–444.

Kuettner, J., 1938: Moazagotl and föhnwalle. *Beitr. Phys. Frei Atmos.,* **25,** 79–114.

——, 1939: Zur entstehung der föhnwalle. *Beitr. Phys. Frei Atmos.,* **25,** 251–299.

——, 1959: The rotor flow in the lee of mountains. Air Force Cambridge Research Center. G.R.D. Research Notes 6, 20 pp.

Laprise, R., and W. R. Peltier, 1989: On the structural characteristics of steady finite-amplitude mountain waves over bell-shaped topography. *J. Atmos. Sci.,* **46,** 586–595.

Lester, P. F., and W. A. Fingerhut, 1974: Lower turbulent zones associated with mountain lee waves. *J. Appl. Meteor.,* **13,** 54–61.

Long, R. R., 1955: Some aspects of the flow of stratified fluids: III. Continuous density gradients. *Tellus,* **7,** 341–357.

Louis, J. F., 1979: A parametric model of vertical eddy fluxes in the atmosphere. *Bound.-Layer Meteor.,* **17,** 187–202.

——, M. Tiedtke, and J. F. Geleyn, 1982: A short history of the operational PBL-parameterization at ECMWF. *Workshop on Planetary Boundary Layer Parameterization,* Reading, United Kingdon, European Centre for Medium-Range Weather Forecasts, 59–79.

Lyra, G., 1943: Theorie der stationären Leewellenstromung in freier Atmosphäre. *Z. Angew. Math. Mech.,* **23,** 1–28.

Mellor, G. L., and T. Yamada, 1974: A hierarchy of turbulence closure models for planetary boundary layers. *J. Atmos. Sci.,* **31,** 1791–1806.

Miller, P. P., and D. R. Durran, 1991: On the sensitivity of downslope windstorms to the asymmetry of the mountain profile. *J. Atmos. Sci.,* **48,** 1457–1473.

Nance, L. B., 1997: On the inclusion of compressibility effects in the Scorer Parameter. *J. Atmos. Sci.,* **54,** 362–367.

——, and D. R. Durran, 1997: A modeling study of nonstationary trapped mountain lee waves. Part I: Mean-flow variability. *J. Atmos. Sci.,* **54,** 2275–2291.

——, and D. R. Durran, 1998: A modeling study of nonstationary trapped mountain lee waves. Part II: Nonlinearity. *J. Atmos. Sci.,* **55,** 1429–1445.

NTSB, 1992: United Airlines Flight 585, Boeing 737-291, N99UA, uncontrolled collision with terrain for uncontrolled reasons, 4 miles south of Colorado Springs, Colorado, March 3, 1991. AAR-92-06, PB92-910407, 160 pp.

Ólafsson, H., and P. Bougeault, 1997: The effect of rotation and surface friction on orographic drag. *J. Atmos. Sci.,* **54,** 193–210.

Orlanski, I., 1976: A simple boundary condition for unbounded hyperbolic flows. *J. Comput. Phys.,* **21,** 251–269.

Panofsky, H. A., and J. A. Dutton, 1984: *Atmospheric Turbulence.* Wiley and Sons, 397 pp.

Pearson, R. A., 1974: Consistent boundary conditions for numerical models of systems that admit dispersive waves. *J. Atmos. Sci.,* **31,** 1481–1489.

Queney, P., G. Corby, N. Gerbier, H. Koschmieder, and J. Zierep, 1960: The airflow over mountains. World Meteorological Organization Tech. Note 34, 135 pp.

Ralph, F. M., J. Neiman, T. L. Keller, D. Levinson, and L. Fedor. 1997: Observations, simulations and analysis of nonstationary trapped lee waves. *J. Atmos. Sci.,* **54,** 1308–1333.

Richard, E., P. Mascart, and E. C. Nickerson, 1989: On the role of surface friction in downslope windstorms. *J. Appl. Meteor.,* **28,** 241–251.

Scorer, R. S., 1955: The theory of airflow over mountains—IV. Separation of flow from the surface. *Quart. J. Roy. Meteor. Soc.,* **81,** 340–350.

Smith, R. B., 1987: Aerial observations of the Yugoslavian Bora. *J. Atmos. Sci.,* **44,** 269–297.

Thompson, W. T., and S. D. Burk, 1991: An investigation of an Arctic front with a vertically nested mesoscale model. *Mon. Wea. Rev.,* **119,** 233–261.

Yamada, T., 1983: Simulations of nocturnal drainage flows by a q^2l turbulence closure model. *J. Atmos. Sci.,* **40,** 91–106.